Available online at www.easd.procedia.org
EASD Procedia EURODYN (2026) 817-836

EASD Procedia

EURODYN 2026
XIII International Conference on Structural Dynamics
M. Beer, C. Papadimitriou, H. Jensen, J. Chen, M. Broggi, J. Behrensdorf (eds.)
Hannover, Germany, 27.09.–01.10 2026

IMPACT OF PAYLOAD AND RIGGING CABLE GEOMETRY ON MULTI-PAYLOAD LIFT DYNAMICS

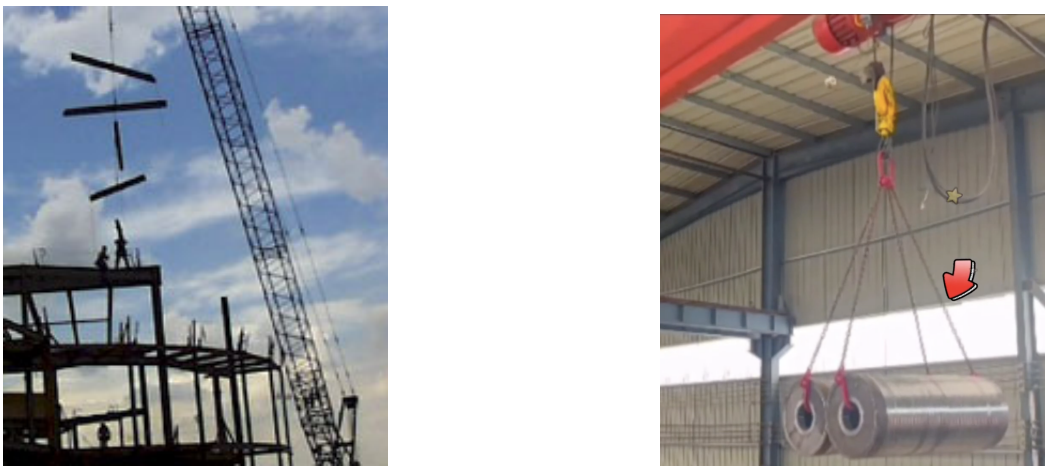
Tyler J. Rome[1], Aldo A. Ferri[1], Christopher J. Adams[1], and William E. Singhose[1]

[1]Georgia Institute of Technology
Atlanta, GA 30318 USA
e-mail: {trome3@,al.ferri@me.,cjadams@,singhose@}gatech.edu

Keywords: Contact, Rolling Contact, Multi-Payload Lift, Crane Dynamics.

Abstract. *Cranes are often used to move large payloads with circular cross sections for use in construction and manufacturing processes. It is well known that movement of these suspended payloads can induce undesirable swing oscillations. However, rolling and sliding frictional contact between payloads and contact between payloads and the environment can also induce undesirable effects. Existing approaches for modeling rolling contact tend to rely either on the restriction of rolling to constant velocity motion or on computationally heavy techniques such as finite-element analysis. Additionally, most existing macroscopic models for rolling contact fail to account for differences in the contact force when examining rolling between two circular bodies versus rolling contact between a circular body and a plane. This work applies a novel model for rolling contact to the simultaneous lifting of multiple circular payloads. Furthermore, an algorithm is proposed for the handling of rolling contact and potential slip when a body has multiple points simultaneously in contact. Simulations investigate the impact of rolling resistance, payload properties, and rigging cable connections on the swing of suspended payloads and the system settling time following a hoist operation. Simulation results indicate that the presence of asymmetry in rigging cable length or payload diameter result in increased outward swing of the payloads and increased settling times.*

ISSN:2311-9020 © 2026 The Authors. Published by EASD Procedia.
Peer-review under responsibility of the Organizing Committee of EURODYN 2026.
doi: 10.47964/1326.10701.564



(a) (b)

Figure 1: Series multi-payload hoist of structural steel members (a) [9] and parallel multi-payload hoist of cylindrical members (b) [10].

1 INTRODUCTION

Cranes play a vital role in numerous construction, shipping, and manufacturing applications; however, these machines possess complex oscillatory dynamics that create challenging control problems for their human operators. In attempts to improve worksite efficiency crews may be instructed to simultaneously hoist multiple loads. However, this simultaneous movement of multiple payloads further increases the complexity of these systems' dynamics, and presents additional safety hazards to those in the surrounding environment. Improving understanding of these complex dynamics provides opportunities to increase operational safety in environments in which cranes are used.

The vast majority of work on modeling and control of suspended payload systems has focused on single and double-pendulum systems involving a single payload or a hook and a payload [1–5], while few prior works have been found that address the simultaneous lift of multiple payloads [6, 7]. However, two potential classes of payload configurations have been identified for these multi-payload lift operations and are defined in this paper as series (or chained/linked) and parallel multi-payload lift operations. In a series multi-payload lift operation the loads are connected in a chain such that each load is suspended from the preceding load in the chain during the hoist operation, as seen in Figure 1a. The larger number of frequency modes present in these higher order suspended pendulum systems introduce additional challenges to the effective control of these crane systems.

To address some of the additional dangers generated by this type of hoist operation the United States Occupational Safety and Health Administration (OSHA) has set limitations on execution of such hoist operations in standard 1926.753 [8]. This standard applies restrictions on aspects of these lift operations such as the maximum number of connected loads, the types of permissible loads, and the length of cable required between each connected load. However, application of this guidance does not remove all risk associated with these move operations.

The second class of multi-payload configurations, which will be investigated further in this paper, involves the suspension of payloads from a single, common point, as seen in Figure 1b. While no published work has been found that examines this payload configuration, incidents that have resulted in injuries and fatalities have been reported following this type of hoist operation [11].

In parallel multi-payload lift operation, the loads may enter into contact with adjacent loads and the surrounding environment. During this contact one, or both, of the contacting bodies will experience some amount of deformation. In the case of identical bodies, this deformation may resemble two circular segments with a shared chord. For modeling of rolling contact between loads with circular cross-sections, additional considerations must be made to account for the dissipation of energy due to rolling resistance. This resistance to rolling motion is generally thought to arise from the asymmetrical distribution of contact stresses along the contact surface and previous work has proposed a model for the "rolling friction coefficient" based on a deformation energy analysis [12]. Additional work with tires has studied the deformation, contact forces, and losses associated with rolling contact using finite element analysis [13–15]; however, this approach tends to be computationally heavy and limiting its practicality in examining numerous different lift conditions. Vozdecký et al. presented a macroscopic approach for modeling rolling contact; however, this analysis was limited to the case of a hard cylindrical object rolling along a deformable incline [16]. This paper will implement a macroscopic model suitable for the case of rolling contact between two loads with circular cross-sections [17].

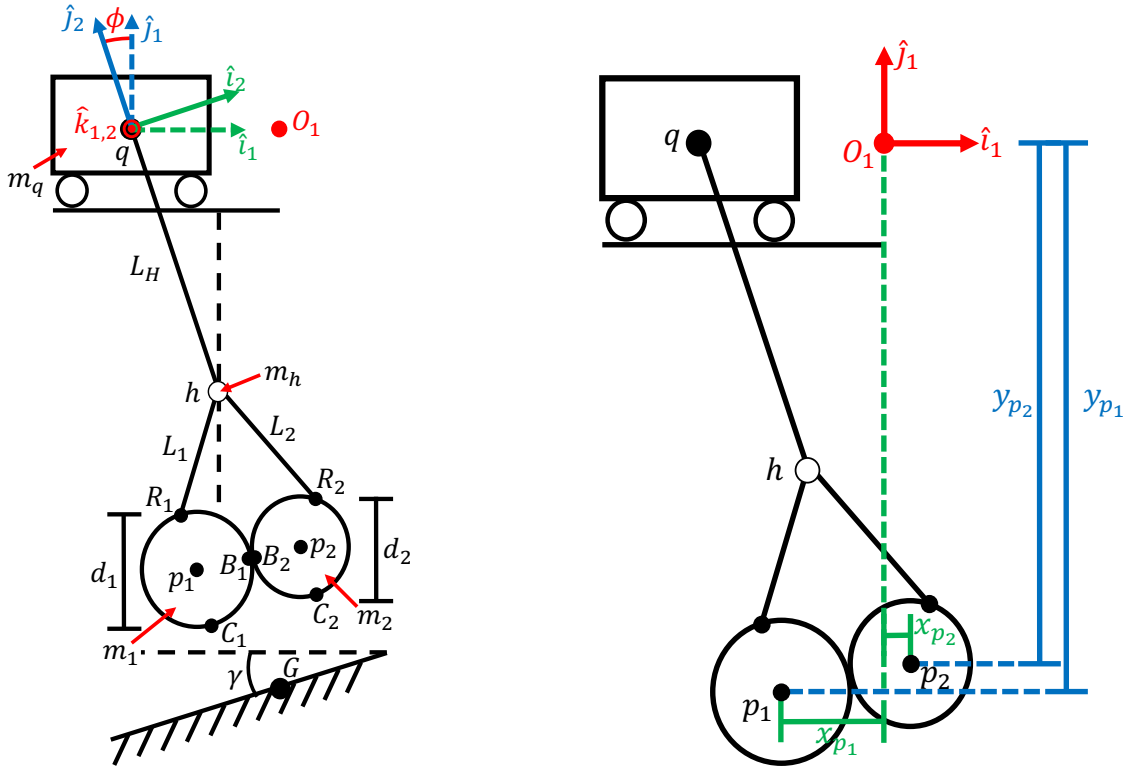
This work develops a model for parallel multi-payload lift operations of payloads with circular cross-sections. This model is used to analyze the impact of payload and rigging cable geometry on the payload out swing and settling time during multi-payload hoist operations. Section 2 presents the 2-dimensional (2D) modeling of a parallel two-circular-payload hoist operation. An algorithm developed to detect slip conditions during the multi-payload hoist is then discussed in Section 3. Next, Section 4 discusses the simulation procedure and analyzes the impact of payload and cable geometry on payload out swing and settling time. Lastly, Section 5 presents the conclusions of this work.

2 SYSTEM MODEL

A system diagram for a two, circular payload lift is shown in Figure 2a. The hook h is suspended from point q on a trolley that may move in the positive and negative $\hat{\imath}_1$ directions. The vectors $\hat{\imath}_S$ and $\hat{\jmath}_S$ are used to define unit vectors parallel to the x- and y-axes of frame S. Thus, the $\hat{\imath}_1$ vector represents the unit vector parallel to the x-axis of the inertial $x_1y_1z_1$ frame whose origin lies at point O_1. Similarly, the $\hat{\jmath}_1$ unit vector is defined to be parallel to the y-axis of the $x_1y_1z_1$ frame. Thus, the absolute position of the suspension point q is defined in the inertial frame by the position vector $\vec{r}_{q/O_1} = x_q\hat{\imath}_1$. The variable x_q represents the displacement of point q from the origin along the inertial x-axis.

2.1 Hook and Hoist Cable

The hook is modeled as a point of mass m_h suspended by a hoist cable of controllable length L_H. As the hoist cable is always in tension due to the weight of the hook, it is chosen to be modeled as a massless, straight link with adjustable length L_H. The $x_2y_2z_2$ frame is selected such that its origin is coincident with the suspension point q and the rigid hoist cable is co-linear with the negative y_2-axis, as seen in Figure 2a. The relative position of the hook from the suspension point in this $x_2y_2z_2$ frame is $\vec{r}_{h/q} = -L_H\hat{\jmath}_2$. The transformation from the $x_2y_2z_2$ reference frame to the inertial reference frame is defined by a rotation ϕ about the z_1/z_2-axis as seen in Figure 2a.



(a) (b)

Figure 2: System diagram for multi-payload lift of two, circular payloads (a) and positions of the payload centroids in the inertial reference frame (b).

2.2 Payloads and Rigging Cables

The positions of the payload centroids p_n for payloads $n = 1, 2$ are defined in the inertial reference frame relative to the origin of the inertial reference frame as seen on the right in Figure 2b. The absolute position of the centroid of payload $n = 1, 2$ is thus defined as $\vec{r}_{p_n/O_1} = x_{p_n}\hat{\imath}_1 + y_{p_n}\hat{\jmath}_1$.

As with the hoist cable, the rigging cables connecting points R_1 and R_2 on payloads 1 and 2 respectively to the hook are treated as massless. However, rather than treating these cables as inextensible rods, it is assumed that these cables are elastic elements that may go slack at certain points during the lift.

Selecting $n = 1, 2$ to the represent payloads 1 and 2 respectively, the lengths of the rigging cables are defined as $L_n = L_{n,0} + \Delta L_n$, where $L_{n,0}$ is the unstretched length of rigging cable n and ΔL_n is the change in length of the rigging cable from the unstretched length. For given spring, K_R, and damping, C_R, coefficients associated with the rigging cables, the tension in the rigging cable n may be expressed as

$$T_n = \begin{cases} K_R\Delta L_n + C_R\Delta\dot{L}_n, & \Delta L_n > 0 \;\&\; \Delta\dot{L}_n > 0 \\ K_R\Delta L_n, & \Delta L_n > 0 \;\&\; \Delta\dot{L}_n \leq 0 \\ 0, & \Delta L_n \leq 0 \end{cases} \tag{1}$$

The time rate of change in rigging cable length, $\Delta\dot{L}_n$, for the multi-payload system is obtained from the difference in velocities of rigging points and hook, $\vec{v}_{h/R_n}$, in the direction of the unit vector parallel to the length of the rigging cable.

The angles of the rigging cables θ_1 and θ_2 are defined relative to the inertial y_1-axis, thus

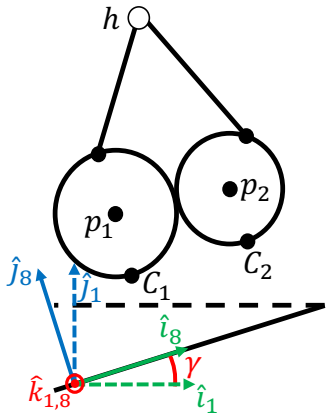


Figure 3: Diagram of unit vectors corresponding to reference frame 8 which is fixed to the ground.

they may be derived from the expression for the relative position vectors from the rigging points to the hook in the inertial reference frame

$$\theta_n = \tan^{-1}\left(-\frac{\vec{r}_{h/R_n}\cdot\hat{\imath}_1}{\vec{r}_{h/R_n}\cdot\hat{\jmath}_1}\right) \tag{2}$$

A negative sign is included within the inverse tangent expression to maintain a positive notation for counter-clockwise rotation of the rigging cables.

2.3 Constraints

In the absence of contact between payloads and between payloads and the environment, the system shown in Figure 2a may be defined with the unconstrained Lagrangian approach and the generalized coordinates $\{q\} = \left\{x_{p_1}\ y_{p_1}\ \beta_1\ x_{p_2}\ y_{p_2}\ \beta_2\ \phi\ L_H\ x_q\right\}^T$. However, there also may be instances in which rolling contact constraints must be applied for the three potential contact pairs 1) Points B_1 and B_2, 2) Point C_1 and the ground, and 3) Point C_2 and the ground.

For rolling contact between the two payloads the velocities of B_1 and B_2 in the direction of the $\hat{\jmath}_7$ unit vector must be equivalent. The $x_7y_7z_7$ frame is fixed to the centroid of payload 1 and rotates about the z_1-axis such that the $\hat{\jmath}_7$ vector is co-linear with the line that passes through the centroids of both payload 1 and payload 2.

The relative position of point B_n from the centroid of payload n in the $x_7y_7z_7$ frame is

$$\vec{r}_{B_n/p_n} = l_B\hat{\imath}_7 \pm h_{B_n}\hat{\jmath}_7 \tag{3}$$

with the addition operation in $\pm$ corresponding to the case of $n = 1$ and the subtraction operation corresponding to $n = 2$. The variable h_{B_n} represents the distance from the centroids of payloads n to the locally deformed contact surfaces during payload-payload contact. The variable l_B represents the distance of the resultant contact force from the center of the locally deformed surface.

For rolling contact between a payload and the ground the velocity of either C_1 or C_2 in the direction of the x_8-axis defined in Figure 3 must be equivalent with the velocity of the ground. The $x_8y_8z_8$ frame is fixed to the ground such that the $\hat{\imath}_8$ unit vector and x_8-axis are co-linear with the surface of the ground.

The relative position of point C_3 from the centroid of payload n in the $x_8y_8z_8$ frame is

$$\vec{r}_{C_n/p_n} = l_{C_n}\hat{\imath}_8 \pm h_{C_n}\hat{\jmath}_8 \tag{4}$$

The variable h_{C_n} represents the distance from the centroid of payload n to the locally deformed contact surfaces during payload-ground contact. The variable l_{C_n} represents the distance of the resultant contact force from the center of the locally deformed surface for payload $n = 1, 2$.

The constraints may then be written in the form

$$[a]\{\dot{q}\} + \{b\} = \{0\} \tag{5}$$

where the vector $\{b\}$ is a three by one vector of zeros. If rolling contact is occurring at all three potential locations the constraint matrix $[a]$ is defined as

$$[a] = \begin{bmatrix} \cos(\alpha) & \sin(\alpha) & -h_{B_1} & -\cos(\alpha) & -\sin(\alpha) & -h_{B_2} & 0 & 0 & 0 \\ \cos(\gamma) & \sin(\gamma) & h_{C_1} & 0 & 0 & 0 & 0 & 0 & 0 \\ 0 & 0 & 0 & \cos(\gamma) & \sin(\gamma) & h_{C_2} & 0 & 0 & 0 \end{bmatrix} \tag{6}$$

As seen in Figure 3, the angle γ in (6) represents the slope of the ground and corresponds to the rotation from the inertial frame to frame 8. While the angle α defines the rotation of the $x_7y_7z_7$ frame and is obtained from the expression

$$\alpha = \tan^{-1}\left(\frac{\vec{r}_{p_2/p_1} \cdot \hat{\imath}_1}{\vec{r}_{p_2/p_1} \cdot \hat{\jmath}_1}\right) \tag{7}$$

The number of rows in the constraint matrix and constraint vector may be reduced depending on whether the no-slip condition requirement holds for the constraint at a given contact pair.

2.4 System Energy

To derive the equations of motion with Lagrange's equation the total kinetic and potential energy of the system is first derived. The total kinetic energy is expressed as

$$E_K = E_{K,hook} + E_{K,p_1} + E_{K,p_2} + E_{K,trolley} \tag{8}$$

Expanding out the expression for the total kinetic energy yields

$$\begin{aligned} E_K = \frac{1}{2}\Big[m_h(L_H^2\dot{\phi}^2 + \dot{L}_H^2 + \dot{x}_q^2) + m_q\dot{x}_q^2 + \dot{\beta}_1^2 I_1 + m_1(\dot{x}_{p_1}^2 + \dot{y}_{p_1}^2) + \dot{\beta}_2^2 I_2 + m_2(\dot{x}_{p_2}^2 + \dot{y}_{p_2}^2)\Big] \\ + m_h\dot{x}_q\dot{\phi}L_H\cos(\phi) + m_h\dot{x}_q\dot{L}_H\sin(\phi) \end{aligned} \tag{9}$$

where m_q, m_h, m_1, and m_2 reflect the masses of the trolley, hook, and two payloads respectively. The variables I_1 and I_2 then represent the moments of inertia associated with payload 1 and 2.

The gravitational forces and elasticity of the rigging cables are incorporated into the generalized forces, thus the total potential energy of the system for the purpose of implementing Lagrange's equation is taken to be zero. The Lagrangian is then taken as the difference in kinetic and potential energy of the entire system.

$$L = E_K - U = E_K \tag{10}$$

2.5 External Forces

The external (non-constraint) forces acting on the hook are found from the free-body diagram in Figure 4. The forces acting on the hook are expressed in vector form as

$$\begin{aligned} \vec{F}_{hook} = &\left[-F_H\sin(\phi) + T_1\sin(\theta_1) + T_2\sin(\theta_2)\right]\hat{\imath}_1 \\ &+ \left[F_H\cos(\phi) - T_1\cos(\theta_1) - T_2\cos(\theta_2) - m_hg\right]\hat{\jmath}_1 \end{aligned} \tag{11}$$

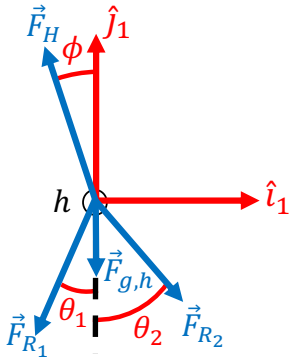
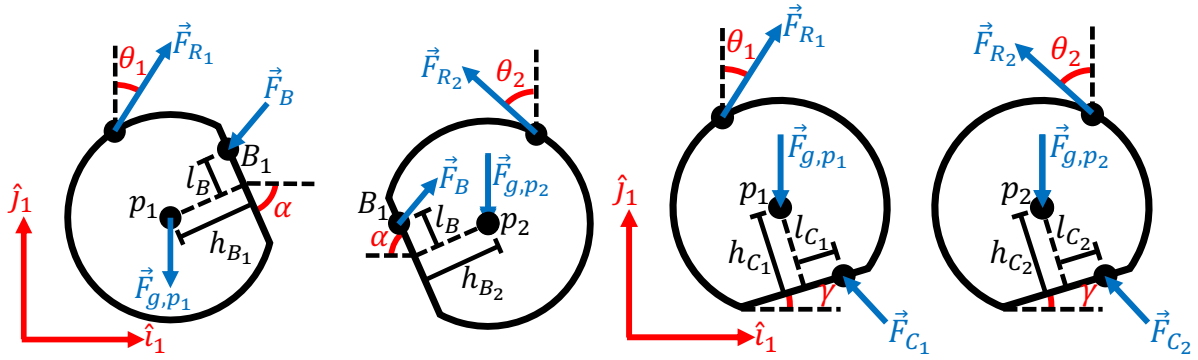


Figure 4: Free-body diagram of the forces acting on the hook.



(a) On payload 1 (left) and payload 2 (right) during payload-payload contact.

(b) On payload 1 (left) and payload 2 (right) during payload-ground contact.

Figure 5: Free-body diagrams of the forces acting on payloads.

The force from the hoist cable on the hook is defined as F_H, while g is the acceleration due to gravity. The tension in rigging cables 1 and 2 are defined as T_1 and T_2 respectively.

The payload-payload contact forces acting on payloads 1 and 2 are shown in Figure 5a alongside the tensile forces from the rigging cables and the gravitational forces acting on the payloads. During payload-ground contact the forces on each payload are defined as shown in Figure 5b.

For determining the equations of motion, the non-constraint forces on payloads are broken into components based on where the forces act on the payload body. The gravitational force is only force acting at the centroid of payloads, thus this force vector is defined as $\vec{F}_{g,p_n} = -m_n g \hat{\jmath}_1$. The forces acting at the rigging point of payload n are described by force vector

$$\vec{F}_{R_n} = -T_n \sin(\theta_n)\hat{\imath}_1 + T_n \cos(\theta_n)\hat{\jmath}_1 \tag{12}$$

The forces at points B_n and C_n on payload $n = 1, 2$ are dependent on whether the no-slip condition holds for the given point. If there is slip between points B_1 and B_2, then

$$\vec{F}_{B_1} = [F_B \sin(\alpha) + f_B \cos(\alpha)]\,\hat{\imath}_1 + [-F_B \cos(\alpha) + f_B \sin(\alpha)]\,\hat{\jmath}_1 \tag{13}$$

where f_B is the kinetic friction between the two bodies at point B_1, F_B is the normal reaction force acting perpendicular to the contact surface of the two payloads, and α is the angle of the contact surface. The force vector acting at B_2 is the negative of (13) by Newton's 3$^{\text{rd}}$ law. If the no-slip condition holds at the point, then the f_B terms equal zero and the force vector for points

B_1 and B_2 is defined solely by the normal reaction force F_B and the angle of the contact surface α. While the force vector acting at C_n during sliding contact is

$$\vec{F}_{C_n} = \left[-F_{C_n}\sin(\gamma) + f_{C_n}\cos(\gamma)\right]\hat{\imath}_1 + \left[F_{C_n}\cos(\gamma) + f_{C_n}\sin(\gamma)\right]\hat{\jmath}_1 \tag{14}$$

The force vector (14) is defined by the normal force between payload n and the ground F_{C_n} and the incline of the ground γ. While f_{C_n} is the kinetic friction force between the payload and the ground. As with no-slip payload-payload contact, the f_{C_n} terms drop from the force vector (14) and contact is solely defined by the normal force between payload n and the ground F_{C_n} and the incline of the ground γ.

2.6 Damping Moments

To address viscous damping losses associated with air drag and contact between cables and connection points, damping moments were introduced into the model. These damping moments are modeled as being linearly proportional to angular velocity. Consequently, for a damping coefficient c_ϕ the damping of the hoist cable is defined as $\vec{D}_h = -c_h\dot{\phi}\hat{k}_1$. Damping of rigging cable n and payload n are similarly defined with damping coefficients c_R and c_p by expressions $\vec{D}_{R_n} = -c_R(\dot{\theta}_n - \dot{\phi})\hat{k}_1$ and $\vec{D}_{p_n} = -c_p(\dot{\beta}_n - \dot{\theta}_n)\hat{k}_1$.

2.7 Generalized Forces

Given the external forces and moments, the generalized force vector is attained through application of the concept of virtual work outlined by Ginsberg [18]. The resultant generalized force vector is

$$\{Q\} = \begin{Bmatrix} Q_{x_{p_1}} & Q_{y_{p_1}} & Q_{\beta_1} & Q_{x_{p_2}} & Q_{y_{p_2}} & Q_{\beta_2} & Q_\phi & Q_{L_H} & Q_{x_q} \end{Bmatrix}^T \tag{15}$$

2.8 Application of the Augmented Method

The Lagrangian (10), the generalized force vector (15), and the constraint equation (5) are then applied to the expression

$$\frac{\partial}{\partial t}\frac{\partial L}{\partial \dot{q}_i} - \frac{\partial L}{\partial q_i} = Q_i + a_i^T\lambda \tag{16}$$

where a_i is the i^{th} column of the constraint matrix (6) and $\{\lambda\}$ is a vector of Lagrange multipliers. This is reorganized into the form $[M(q,t)]\{\ddot{q}\} = [a]^T\{\lambda\} + \{F\}$ where $[M(q,t)]$ is a mass matrix associated with the coefficients of the $\{\ddot{q}\}$ terms in (16) and $\{F\}$ is a column vector of the generalized forces and any of the remaining terms from the left-hand side of (16) that were not incorporated into $[M(q,t)]$. The mass matrix comes out to

$$[M(q,t)] = \begin{bmatrix} [M_1]_{6\times6} & [0]_{6\times3} \\ [0]_{3\times6} & [M_2]_{3\times3} \end{bmatrix} \tag{17}$$

with

$$[M_1] = \text{diag}(m_1, m_1, I_1, m_2, m_2, I_2) \tag{18}$$

and

$$[M_2] = \begin{bmatrix} m_h L_H^2 & 0 & m_h L_H\cos(\phi) \\ 0 & m_h & m_h\sin(\phi) \\ m_h L_H\cos(\phi) & m_h\sin(\phi) & m_h + m_q \end{bmatrix} \tag{19}$$

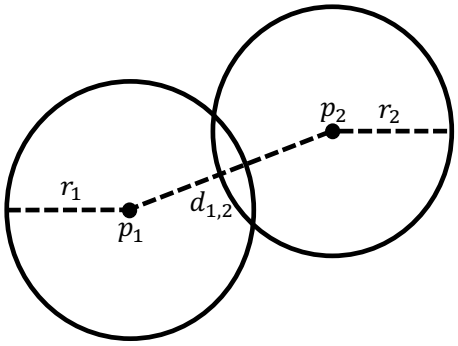


Figure 6: Payload-payload contact diagram showing overlap of payload areas during contact.

While the F vector is found to be

$$\{F\} = \{Q\} + \begin{Bmatrix} \{0\}_{6\times1} \\ 2L_H\dot{L}_H\dot{\phi}m_h \\ -L_H\dot{\phi}^2m_h \\ -m_h\dot{\phi}(\dot{\phi}\sin(\phi)L_H - 2\cos(\phi)\dot{L}_H) \end{Bmatrix} \tag{20}$$

where $\{0\}_{6\times1}$ is a 6×1 vector of zeros. The equations of motion are then put into the augmented form

$$\begin{Bmatrix} \ddot{q} \\ \lambda \end{Bmatrix} = \begin{bmatrix} M(q,t) & -a^T \\ -a & 0 \end{bmatrix}^{-1} \begin{Bmatrix} F \\ S \end{Bmatrix} \tag{21}$$

where $\{S\}$ is defined as

$$\{S\} = \left[\frac{da}{dt}\right]\{\dot{q}\} + \left\{\frac{db}{dt}\right\} \tag{22}$$

The equations of motion vary depending on the number of no-slip constraints that are not violated.

2.9 Contact Detection

To model the lift of a multi-payload system as seen in Figure 2a, it is necessary to detect when payloads are in contact with each other and when they are in contact with the surrounding environment.

For payload-payload contact detection in 2D, it is sufficient to check that the distance between the centroids of the two payloads is less than the sum of the payloads' radii. An example of payload-payload contact is shown in Figure 6 where the distance between the payload centroids $d_{1,2}$ is less than the sum of the radii r_1 and r_2. This can be expressed by the equations

$$\delta_B = (y_{p_2} - y_{p_1})\cos(\alpha) + \sin(\alpha)(x_{p_1} - x_{p_2}) - (r_1 + r_2) \tag{23}$$

where a negative δ_B indicates contact between the payloads.

For payload-ground contact in 2D, it is sufficient to show that the distance from the centroid to the closest point on the ground is less than the radius of the payload. Given the relative position of point G on the ground from the origin of the inertial reference frame is defined as $\vec{r}_{G/O_1} = -L_G\hat{j}_1$.

The difference in the payload radius and the distance between the payload centroid and ground is found through the expression

$$\delta_{C_n} = (L_G + y_{p_n})\cos(\gamma) - x_{p_n}\sin(\gamma) - r_n \tag{24}$$

As with the payload-payload contact case, a negative δ_{C_n} indicates contact between payload n and the ground.

2.10 Resultant Contact Force Locations

The locations of the resultant contact forces during contact are then defined by the relative position vectors $\vec{r}_{B_1/p_1}$ and $\vec{r}_{B_2/p_2}$. The values of the locally deformed radii h_{B_1}, h_{B_2}, h_{C_1}, and h_{C_2} depend on the diameters and material properties of the payloads and ground. These values are restricted to be between 0 and the radius of their respective payload, thus $0 \leq h_{B_n} \leq r_n$ and $0 \leq h_{C_n} \leq r_n$.

The value of the deformed local radius h_{B_1} may be expressed as

$$h_{B_1} = \begin{cases} r_1 + \delta_B \eta, & \delta_B < 0 \\ r_1 \quad , & \delta_B \geq 0 \end{cases} \tag{25}$$

where η is a value between 0 and 1 that reflects the local deformation of payload 1 relative to the total local deformation. In the expression for the deformed local radius h_{B_2}, the η in (25) is replaced with a $1 - \eta$ term. The deformation of the payloads is assumed to be identical in this work, and thus $\eta = 0.5$.

For contact with the ground, it is assumed that the ground is a rigid, non-deformable surface thus the locally deformed radii for payload-ground contact are defined as

$$h_{C_n} = \begin{cases} r_n + \delta_{C_n}, & \delta_B < 0 \\ r_n \quad , & \delta_B \geq 0 \end{cases} \tag{26}$$

The distance of the resultant contact force from the center of the contact surface during payload-payload contact is expressed as a function of the payload undeformed and deformed radii and a scaling value c_B between -1 and 1.

$$l_B = c_B \sqrt{r_1^2 - h_{B_1}^2} = c_B \sqrt{r_2^2 - h_{B_2}^2} \tag{27}$$

Given the complex nature of rolling contact, c_B may in general depend on a number of parameters associated with velocity, loading, geometry, material properties, etc. It is assumed the dependence is limited to the difference in angular velocity and selected such that the distance l_B approaches zero as the difference in angular velocities approaches zero

$$c_B = -C_B \tanh\left(\frac{\dot{\beta}_2 - \dot{\beta}_1}{\epsilon_\omega}\right) \tag{28}$$

In this expression ϵ_ω is a small value and C_B is a simplified scaling factor between 0 and 1 that influences that maximum distance a resultant contact force can be from the center of the contact surface. In this work the value of C_B is selected to investigate the impact of resultant force location on system behavior. Similar expressions are derived for the distances of the resultant contact force during payload-ground contact l_{C_1} and l_{C_2}.

It is worth noting that if the local deformation δ_B and δ_{C_n} are significantly smaller than the payload radii, then the locally deformed radii can be reasonably approximated as the undeformed radii. Additionally, it is worth noting that while the selected expressions for l_B and c_B drive the resultant contact force to the center of the contact surface when there is zero rotational motion, it does not necessarily encapsulate all properties that may influence the value of l_B.

2.11 Normal Contact Forces

The normal contact force between two elastic spherical bodies may be reasonably approximated with Hertzian contact

$$F_n = -K\delta_n^{\frac{3}{2}} \tag{29}$$

The contact stiffness K is defined as a function of the bodies' radii, the bodies' Young's modulus, and the bodies Poisson's ratio [19].

A number of papers have presented contact force models between non-elastic spheres [19–22]. However, these models are reliant on a non-zero initial contact velocity, thus their use is limited when the bodies start in contact. For this work a simpler dissipative normal force model is implemented

$$F_n = \begin{cases} -K\delta_n^{\frac{3}{2}} - C\dot{\delta}_n, & \delta_n \leq 0 \;\&\; \dot{\delta}_n \leq 0 \\ -K\delta_n^{\frac{3}{2}}, & \delta_n \leq 0 \;\&\; \dot{\delta}_n > 0 \\ 0, & \delta_n > 0 \end{cases} \tag{30}$$

Where C represents the damping coefficient during the compression phase of contact. While this approach does present a discontinuity at $\delta_n = 0$ and $\dot{\delta}_n > 0$, it is not reliant on an initial contact velocity.

2.12 Kinetic Friction

In the case of contact with slip it is necessary to calculate the kinetic friction acting on the contact surface. This kinetic friction for contact between payloads is expressed as $f_{B,k} = \mu_{k_p} F_B$ where μ_{k_p} is the coefficient of kinetic friction for the two contacting surfaces. The kinetic friction for contact between either of the payloads and the ground is similarly defined for kinetic friction coefficient μ_{k_G} and normal contact force F_{C_n}.

3 SLIP DETECTION ALGORITHM

To check the validity of the constraints, the potential contact points are checked to inspect if contact is occurring at the given point. The process for checking contact between bodies is detailed in Section 2.9.

If a pair of points is in contact, then it is examined if the relative velocity of the two points in the direction parallel to the contact surface is less than 10^{-5} m/s. If this condition holds, then it is assumed there is the potential for the no-slip condition to be satisfied. This is done to account for any potential floating point errors when comparing the velocities.

Moving forward with the current assumption that any pair of points with a relative velocity difference less than 10^{-5} m/s experiences rolling contact, the static friction component of each reaction force is calculated. If any of the contact pairs has a static friction component greater than the permissible static friction limit based on the static friction coefficient and normal force between the two bodies, then the difference between calculated and permissible static friction is calculated.

The maximum permissible static friction for payload-payload contact is defined as $f_{B,s} = \mu_{s_p} F_B$ where μ_{s_p} is the coefficient of static friction for the two contacting surfaces. While the maximum permissible static friction for payload-ground contact with static friction coefficient μ_{s_G} is defined as $f_{C_n,s} = \mu_{s_G} F_{C_n}$.

The pair of points with the largest difference in calculated and permissible static friction is assumed to have slipped and the tangential components of the reaction forces are recalculated. This is repeated until none of the contact pairs violate the maximum permissible static friction.

Once the validity of the assumed no-slip conditions is verified, the equations of motion for the constrained system are calculated from (21). The number of rows in the $[a]$ and $\frac{d}{dt}[a]$ matrices as well as the $\frac{d}{dt}\{b\}$ vector is dependent on the number of remaining valid no-slip contact conditions.

Table 1: Simulation parameters.

Parameter	Variable	Value
Trolley Mass	m_q	100 [kg]
Hook Mass	m_h	20 [kg]
Payload Density	ρ	2700 [kg·m^2]
Hook Damping Coefficient	c_h	170 [N·m·s]
Rigging Damping Coefficient	c_R	5 [N·m·s]
Payload Damping Coefficient	c_p	2 [N·m·s]
Rigging Cable Spring Coefficient	K_R	$50{\cdot}10^8$ [N/m]
Rigging Cable Damping Coefficient	C_R	10^5 [N·s/m]
Equivalent Elastic Modulus	E	$3.87{\cdot}10^{10}$ [N/m^2]
Contact Damping Coefficient	C	10^6 [kg/s]
Payload-Payload Static Friction Coefficient	μ_{s_p}	0.4 [unitless]
Payload-Payload Kinetic Friction Coefficient	μ_{k_p}	0.4 [unitless]
Payload-Ground Static Friction Coefficient	μ_{s_G}	0.4 [unitless]
Payload-Ground Kinetic Friction Coefficient	μ_{k_G}	0.35 [unitless]
Resultant Force Location Scaling Constant	ϵ_ω	0.002 [unitless]

4 SIMULATION OF MULTI-PAYLOAD HOIST CONFIGURATIONS

Simulations were performed in MATLAB to investigate the impact of payload and rigging geometry on system settling time and sideways out swing of the payloads during hoisting operations. In the first set of simulated lift operations, the payload diameters were varied independently from 1 m to 1.5 m, while the unstretched rigging cable lengths were specified to be equivalent and varied from 0.5 m to 1.5 m. In the second set of lift operations, the payloads were restricted to have equivalent diameters that were varied from 1 m to 1.5 m, while the unstretched rigging cable lengths were independently varied from 0.5 m to 1.5 m. The payloads were modeled as cylindrical tubes with a wall thickness of 0.1 m. Consequently, the moment of inertia for payload $n = 1, 2$ is defined by the expression

$$I_n = 0.5 m_n \left[\left(\frac{d_n}{2} \right)^2 + \left(\frac{i_n}{2} \right)^2 \right] \tag{31}$$

where i_n is the interior diameter of payload n given by $i_n = d_n - 0.2$. The remaining system parameters are detailed in Table 1.

Due to the symmetry in rigging cable lengths for the first set of lift operations, only configurations in which $d_1 \leq d_2$ were examined for the first set of lift operations. Similarly, due to symmetry of payload diameters in the second set of lift operations, only configurations in which $L_1 \leq L_2$ were examined.

4.1 Simulation Initial Conditions and Input Commands

In the simulated trials examined in this work, the trolley's $\hat{\imath}_1$ position was fixed at a value of $x_q = 0$. A 14-second trapezoidal profile with a maximum velocity of 0.2 m/s and a ramp acceleration of 0.1 m/s^2 was applied to the hoist input to lift the payloads in the various size configurations. The initial $\hat{\jmath}_1$ position of the payloads' centroids was selected for each configu-

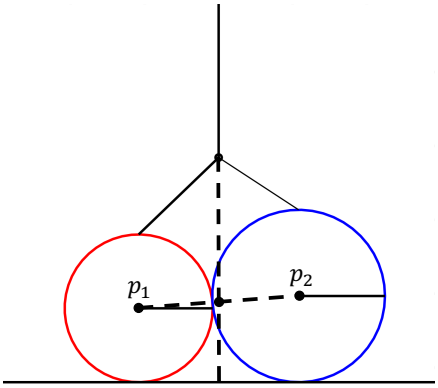


Figure 7: Initial system configuration for one potential combination of payload diameters and rigging lengths.

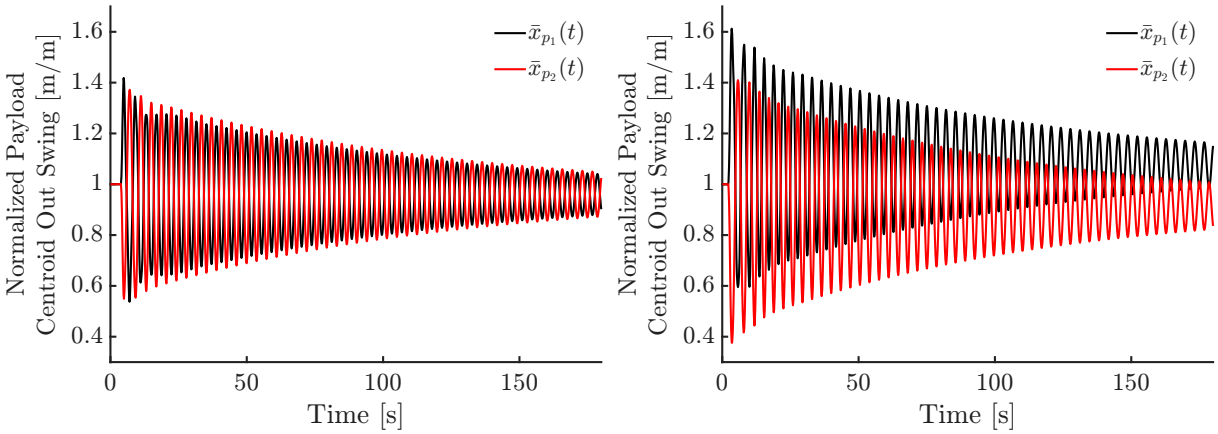
ration of payload diameters such that penetration between the payload and the ground resulted in a normal component of the resultant ground contact force equivalent to the gravitational force acting on the payload. The initial $\hat{\imath}_1$ component of the payloads' centroid positions was then specified such that the mid-point of the line between the two centroids fell directly below the suspension point q on the trolley, as seen in Figure 7. The initial angular rotation of the payloads was set to zero such that the rigging points R_1 and R_2 were positioned directly above the payload centroids. The initial hoist cable offset angle ϕ was set to zero, while the length of the hoist cable L_H was defined as the minimum length before which either of the rigging cables would stretch beyond their initial lengths. The resultant force location scaling factor C_B was then set to a value of 0.5.

To ensure the initial conditions were correctly applied, such that both payloads started at rest, the response of the system was simulated for a duration of 1 second before the trapezoidal hoist velocity profile was applied to the system.

4.2 System Out Swing During Lift

As seen in Figure 8a, asymmetry in the rigging cable lengths may generate conditions in which the $\hat{\imath}_1$ component of the payloads' position varies from the initial conditions resulting in an outward swing motion. The normalized outward swing of the payload centroid, $\bar{x}_{p_n}(t)$, for payload $n = 1, 2$ is defined as the current $\hat{\imath}_1$ component of the position of payload n's centroid, $x_{p_n}(t)$, divided by its initial value $x_{p_n}(0)$. In the case seen in Figure 8a, the asymmetry results in an initial large increase in the normalized swing of payload 1 corresponding to a large outward swing and an initial decrease in normalized swing of payload 2 corresponding to an inward swing. The amplitude of the initial out swing of payload 1 is slightly larger than that of payload 2; however, as the swing decays this relationship flips and the amplitude of the payload 2 centroid swing remains larger than the amplitude of the payload 1 centroid swing. Additionally, after application of the hoist command, the equilibrium value of the payload normalized centroid out swing is less than 1 for both payloads. This indicates that at rest the $\hat{\imath}_1$ distance between the centroids of both payloads and the trolley is less than the $\hat{\imath}_1$ distance between these points prior to the start of the hoist operation.

For a system configuration of $d_1 = 1\text{m}$, $d_2 = 1.1667\text{m}$, $L_{1,0} = 0.75\text{m}$, and $L_{2,0} = 0.75\text{m}$, the disparity in payload diameters results in a large initial outward swing of payload 1 as seen in Figure 8b. Additionally, the equilibrium value of the normalized payload centroid out swing for payload 1 is greater than 1 for this system configuration, while the equilibrium value for the normalized out swing of payload 2 is less than 1. This result indicates that both centroids will



(a) Case of $d_1 = 1$m, $d_2 = 1$m, $L_{1,0} = 0.5$m, and $L_{2,0} = 0.75$m.

(b) Case of $d_1 = 1$m, $d_2 = 1.1667$m, $L_{1,0} = 0.75$m, and $L_{2,0} = 0.75$m.

Figure 8: Time history data of payload centroid $\hat{\imath}_1$ components normalized by the initial offset from the suspension point.

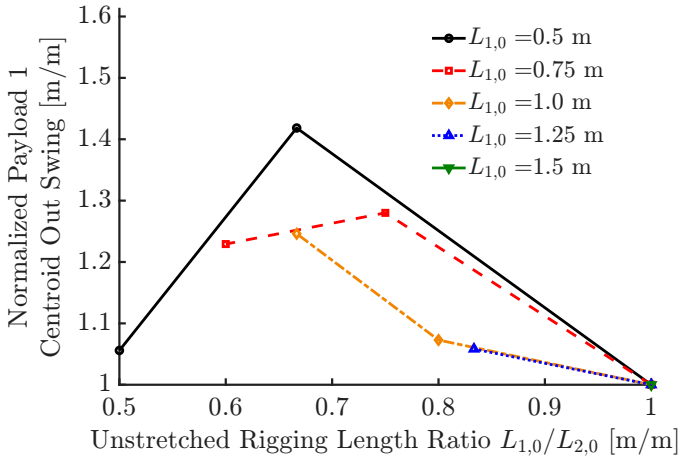


Figure 9: Normalized peak out swing of payload 1 centroid versus ratio of rigging cable lengths for $d_1 = 1$m and $d_2 = 1$m.

lie to the right of their initial starting points once equilibrium is reached.

As observed in Figure 8, the magnitude of the out swing was observed to vary significantly with the geometry of the payload's and rigging cables. As seen in Figure 9 for the case of $d_1 = 1$m and $d_2 = 1$m, the normalized out swing of payload 1 increases as the difference in unstretched length of the two rigging cables begins to increase. However, for the cases of $L_{1,0} = 0.5$m and 0.75m, the normalized out swing decreased after the $L_{2,0}$ value was increased to 1m and 1.25m respectively.

Likewise, in configurations with symmetric unstretched rigging cable lengths, asymmetry in the payload diameters resulted in an increase in the maximum outward swing of payload 1 as seen in Figure 10. The rate at which the normalized payload out swing increased was seen to increase as the diameter of payload 1 increased.

Additionally, near a payload diameter ratio of 1, the rate at which payload out swing increased with payload diameter asymmetry was seen to decrease as the unstretched length of the rigging cables was increased. This behavior suggests that if small asymmetries in payload diameter are present, then it may be possible to reduce the potential outward swing of the payloads by increasing the unstretched length of the rigging cables.

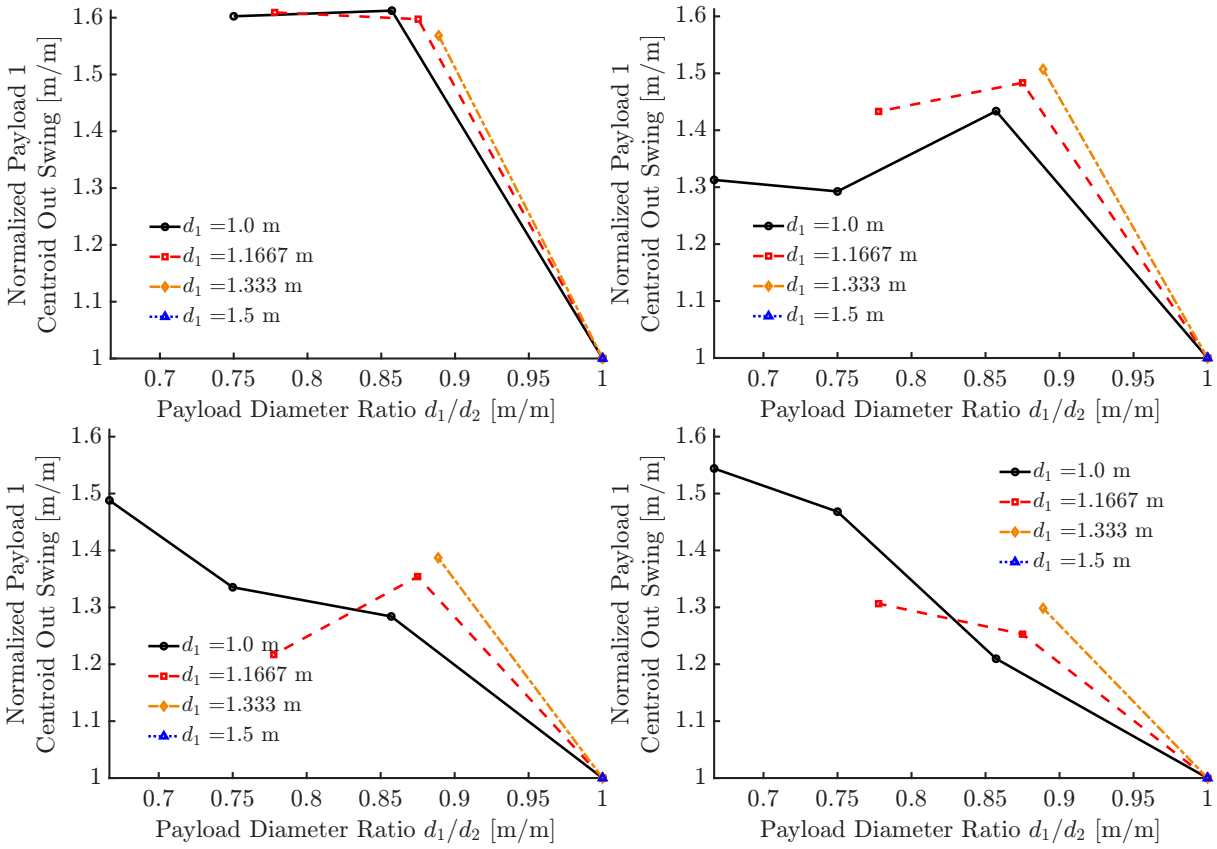


Figure 10: Normalized peak out swing of payload 1 centroid versus ratio of payload diameters for L_1, L_2 = 0.75m (top left), L_1, L_2 = 1m (top right), L_1, L_2 = 1.25m (bottom left), and L_1, L_2 = 1.5m (bottom right).

4.3 System Settling Time

In addition to outward payload swing, the response of the system under varying rigging and payload geometries may be evaluated through examination of the settling times of the system. In this work the settling time was taken as the time from the end of the hoist input command until the system's kinetic energy remained below 5% of the maximum kinetic energy experienced during the residual oscillation phase. Analysis of the varying geometry scenarios indicated that in cases with equivalent rigging lengths and payload diameters the kinetic energy of the system settled to within 5% of the maximum experienced residual kinetic energy within on average 22.45 seconds with a standard deviation of 8.58 seconds. During scenarios in which payload diameters and unstretched rigging lengths are respectively equal the settling time is dominated by the resistance to rolling motion between the two payloads. This behavior is observed in Figure 11 for the configuration d_1 = 1m, d_2 = 1m, $L_{1,0}$ = 1m, and $L_{2,0}$ = 1m.

The decay envelope of the kinetic energy is plotted for five different values of the resultant force location scaling factor C_B, ranging from 0, where the resultant force is restricted to the center of the contact surface, up to 1, where the value of l_B caps out at half the length of the contact surface. Increases in the scaling factor resulted in greater resistance to the rolling motion between the payloads and faster settling. Additionally, the initial peak kinetic energy during the residual oscillation phase is shown to decrease as the scaling factor increased. This indicates that, as expected, increases in rolling resistance additionally result in larger amounts of energy dissipation during the transient phase.

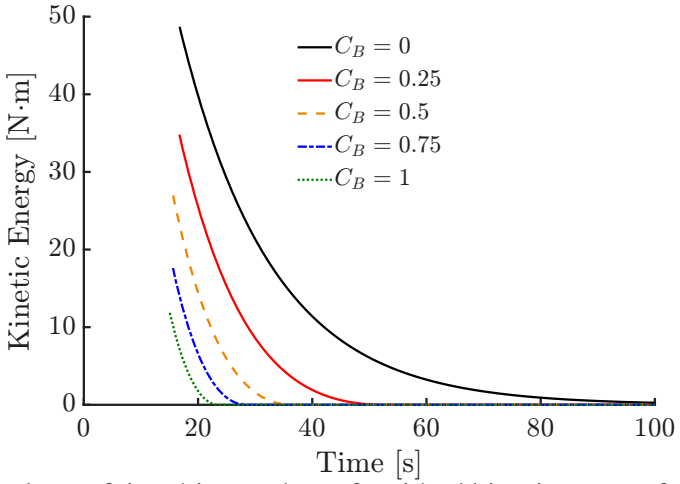


Figure 11: Decay envelope of time history data of residual kinetic energy for the case of d_1 = 1m, d_2 = 1m, $L_{1,0}$ = 1m, and $L_{2,0}$ = 1m and varying values of the resultant force location scaling factor C_B.

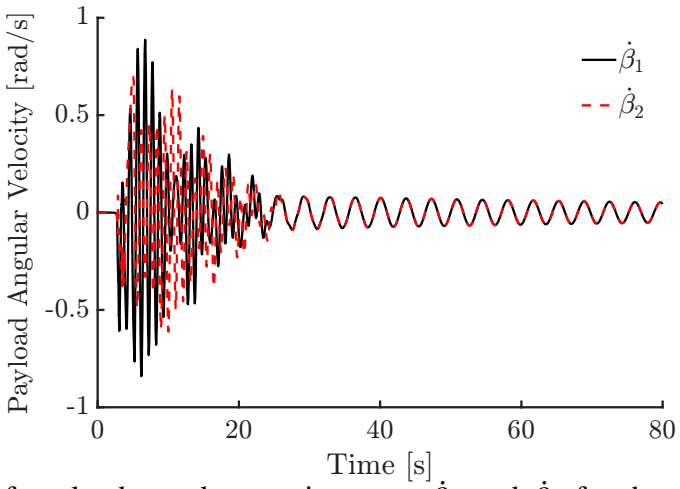


Figure 12: Decay of payload angular rotation rates $\dot{\beta}_1$ and $\dot{\beta}_2$ for the configuration case of d_1 = 1m, d_2 = 1m, $L_{1,0}$ = 0.75m, and $L_{2,0}$ = 1.25m.

However, in cases in which there was asymmetry in the payload and/or rigging geometry, oscillations persisted in the system even after the difference in angular velocities of the payloads reaches zero as seen in Figure 12. In these cases the relative rotation between the payloads quickly decayed while swinging motion associated with the coordinate ϕ persists. For the equal payload diameter configurations in the first set of lift operations, the average settling time for configurations with unequal unstretched rigging lengths was 301.50 seconds with a standard deviation of 180.55 seconds. The large standard deviation for the set of lift operations with equal diameters and unequal rigging lengths may be in part attributed to the increase in settling time with increases in payload diameter and inertia seen in Figure 13. However, significant variance in settling time was also observed due to changes in the asymmetry of the unstretched rigging cable lengths. In the cases of $L_{1,0}/L_{2,0}$ = 0.5 for payload diameters greater than 1m, one payload remained in contact with the ground for a large portion of the hoist operation. The resulting frictional contact with the ground removed large amounts of energy from the system. As a result, at the end of the hoist command very little oscillatory swing kinetic energy remained in the system.

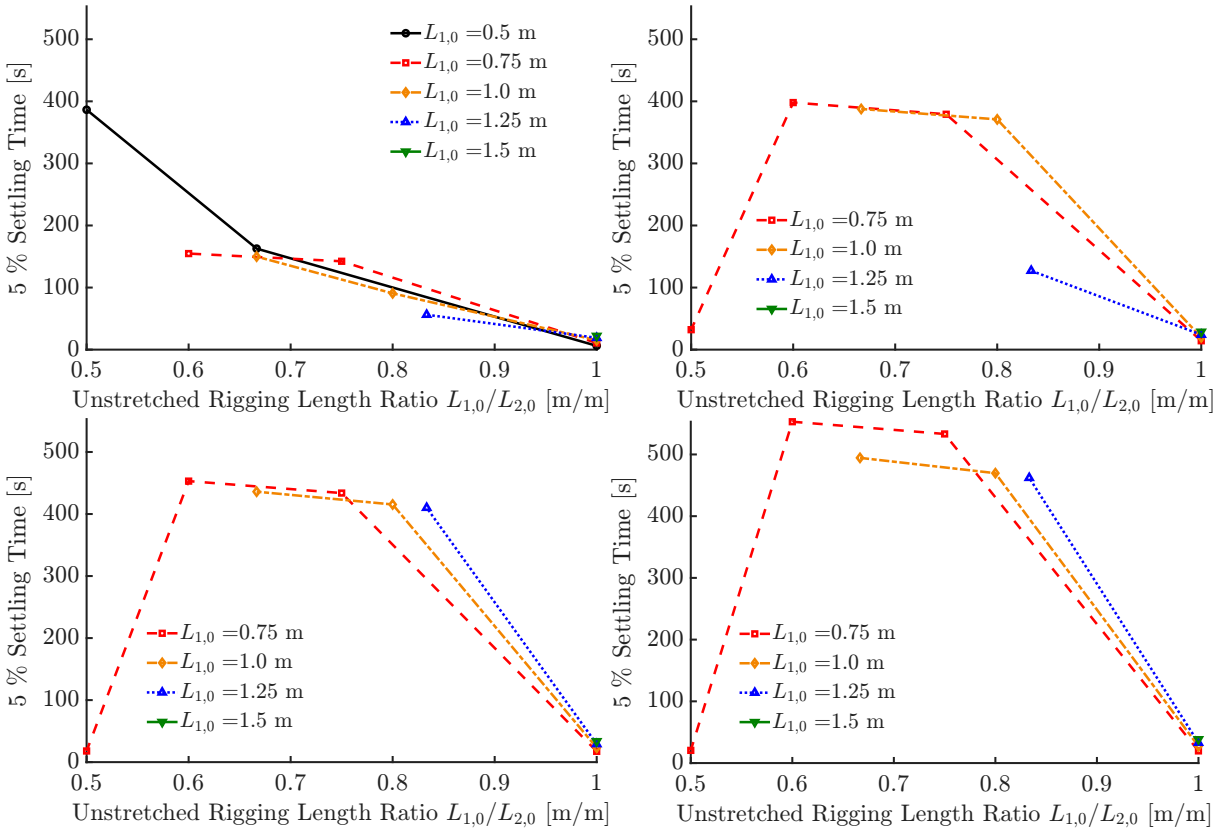


Figure 13: 5% settling time versus ratio of rigging cable lengths for d_1, d_2 = 1m (top left), d_1, d_2 = 1.1667m (top right), d_1, d_2 = 1.333m (bottom left), and d_1, d_2 = 1.5m (bottom right).

For equal rigging cables and unequal payload diameters, this average settling time jumped to 346.13 seconds. As seen in Figure 14, the settling time generally increased as the difference in payload diameters increased. This behavior alongside the variance in settling time with payload diameter contributed to a large standard deviation of 107.14 seconds.

5 CONCLUSIONS

A novel approach to modeling rolling resistance between contacting bodies was applied to the simultaneous lifting of cylindrical payloads. Additionally, an algorithm was implemented to predict rolling contact and potential slip when contact with a body occurs at multiple points. These methods were used to investigate the impact of changes in payload geometry and rigging length on maximum out swing of the hoisted payloads and the system settling time.

While scenarios in which the geometries of the payloads and rigging cables were defined to be equivalent had consistently low levels of settling times and approximately zero outward swing of the payloads during lift, significant variance in both settling time and out swing were observed in cases in which the geometries of the payload/rigging cable pairs varied. While the tested geometries do not encompass all potential payload diameter and unstretched rigging length pairs, the results do suggest that any deviation from a symmetric payload/rigging cable configuration is likely to result in larger settling times and increases in the outward swing of payloads resulting from the hoist operation.

Several asymmetric combinations of payload diameters and rigging lengths were found to produce low levels of outward payload swing and/or small settling times. However, due to the

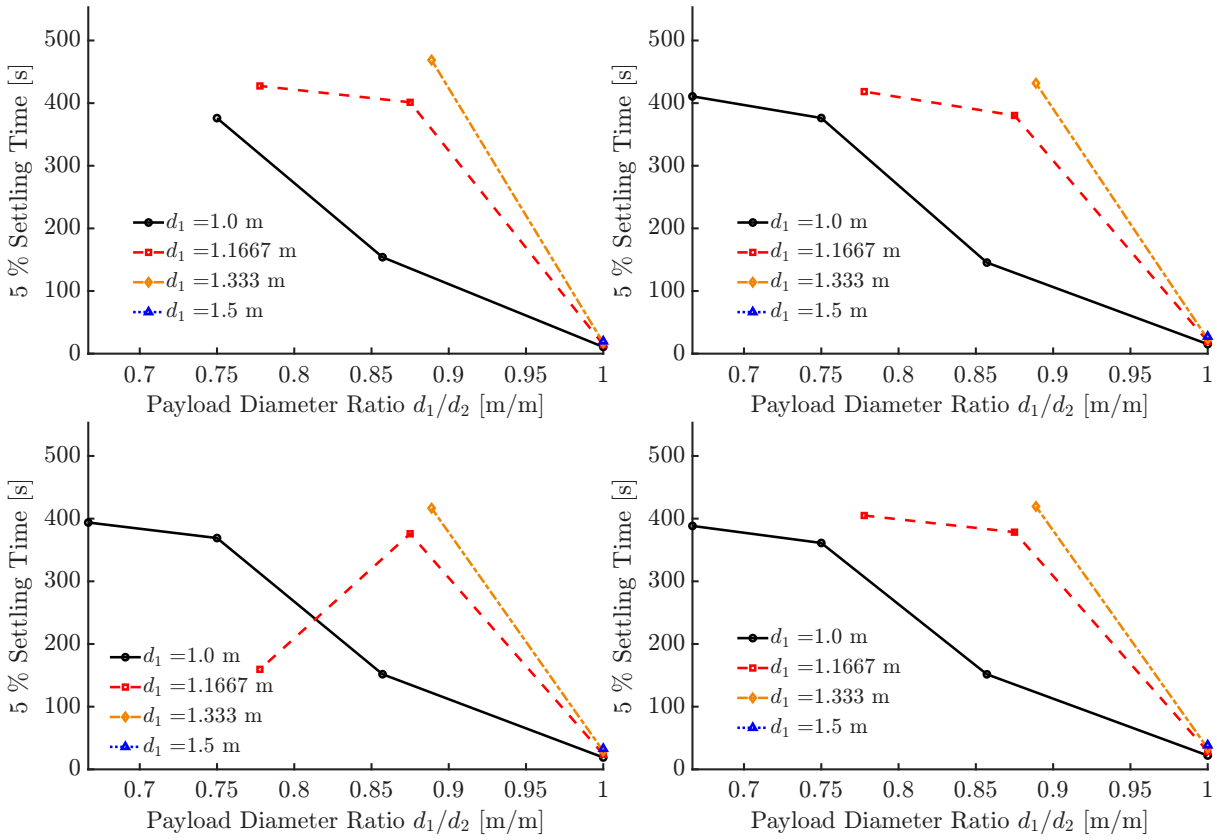


Figure 14: Ratio of payload diameters versus 5% settling time for $L_1, L_2 = 0.75$m (top left), $L_1, L_2 = 1$m (top right), $L_1, L_2 = 1.25$m (bottom left), and $L_1, L_2 = 1.5$m (bottom right).

stark difference in response behavior between symmetric and asymmetric cases, it is suggested that future work investigate the impact of minor asymmetries on the outward swing and settling time of these parallel multi-payload hoist operations. Furthermore, investigation of the impact of rigging cable length in cases of asymmetric payloads suggests that reduction in outward swing of payloads may be achieved through use of longer rigging cables.

Lastly, through modification of the rolling resistance scaling factor C_B, the location of the resultant contact force during rolling contact was observed to have a significant impact on settling time for systems in which the two payloads and rigging cables were equivalent.

ACKNOWLEDGEMENTS

Support for this work was provided by the Sarah Pantip Wong Family through the Crane Safety Research Center at Georgia Tech.

REFERENCES

[1] William Singhose et al. “Effects of hoisting on the input shaping control of gantry cranes”. In: *Control Engineering Practice* 8.10 (2000), pp. 1159–1165. ISSN: 0967-0661. DOI: https://doi.org/10.1016/S0967-0661(00)00054-X.

[2] Chung Choo Chung and John Hauser. “Nonlinear control of a swinging pendulum”. In: *Automatica* 31.6 (1995), pp. 851–862. ISSN: 0005-1098. DOI: https://doi.org/10.1016/0005-1098(94)00148-C.

[3] Qingxiang Wu et al. "Dynamic analysis and time optimal anti-swing control of double pendulum bridge crane with distributed mass beams". In: *Mechanical Systems and Signal Processing* 144 (2020), p. 106968. ISSN: 0888-3270. DOI: https://doi.org/10.1016/j.ymssp.2020.106968.

[4] Joshua Vaughan, Dooroo Kim, and William Singhose. "Control of Tower Cranes With Double-Pendulum Payload Dynamics". In: *IEEE Transactions on Control Systems Technology* 18.6 (2010), pp. 1345–1358. DOI: 10.1109/TCST.2010.2040178.

[5] Robert Mar et al. "Combined input shaping and feedback control for double-pendulum systems". In: *Mechanical Systems and Signal Processing* 85 (2017), pp. 267–277. ISSN: 0888-3270. DOI: https://doi.org/10.1016/j.ymssp.2016.08.012.

[6] Qingxiang Wu, Ning Sun, and Tong Yang. "Model-Free Control of Triple Pendulum Crane Systems with Distributed Mass Payloads". In: *Advances in Guidance, Navigation and Control*. Ed. by Liang Yan, Haibin Duan, and Yimin Deng. Singapore: Springer Nature Singapore, 2025, pp. 113–117. ISBN: 978-981-96-2240-5.

[7] Xin Xin, Jing Pan, and Bin Xu. "Coupling-Energy-Based Antiswing PD Control for a General n-Link Pendulum–Cart System: Theory and Experimental Validation". In: *IEEE Transactions on Industrial Electronics* 72.6 (2025), pp. 6194–6204. DOI: 10.1109/TIE.2024.3497297.

[8] U.S. Department of Labor. *1926.753 - Hoisting and rigging*. URL: https://www.osha.gov/laws-regs/regulations/standardnumber/1926/1926.753.

[9] U.S. Department of Labor. *Steel Erection - Cranes*. 2026. URL: https://www.osha.gov/etools/steel-erection/cranes.

[10] YT Overhead Cranes, Hoists Types, and Installation. *Overhead Crane Anti Swing and Swing Control for Precision and Efficiency- Custom Antiswing Crane*. Oct. 2022. URL: https://www.youtube.com/watch?v=ussrf9HfqfI.

[11] CBS. *Construction Worker Killed By Falling Debris At MIT*. Feb. 2019. URL: https://www.cbsnews.com/boston/news/3-construction-workers-hurt-falling-debris-mit/.

[12] R H Norman. "The rolling friction of cylinders on planes". In: *British Journal of Applied Physics* 13.7 (July 1962), p. 358. DOI: 10.1088/0508-3443/13/7/320.

[13] P Ghosh, A Saha, and R Mukhopadhyay. "Prediction of tyre rolling resistance using FEA". In: *Constitutive Models for Rubber III*. CRC Press, 2003, pp. 141–145.

[14] David E. Hall and J. Cal Moreland. "Fundamentals of Rolling Resistance". In: *Rubber Chemistry and Technology* 74.3 (July 2001), pp. 525–539. ISSN: 0035-9475. DOI: 10.5254/1.3547650.

[15] J. R. Cho et al. "Finite element estimation of hysteretic loss and rolling resistance of 3-D patterned tire". In: *International Journal of Mechanics and Materials in Design* 9.4 (2013), pp. 355–366. DOI: 10.1007/s10999-013-9225-y.

[16] L Vozdecký, J Bartoš, and J Musilová. "Rolling friction—models and experiment. An undergraduate student project". In: *European Journal of Physics* 35.5 (June 2014), p. 055004. DOI: 10.1088/0143-0807/35/5/055004.

[17] Tyler Rome et al. “Rolling Resistance Model for Deformable Bodies With No Slip”. In: *Journal of Computational and Nonlinear Dynamics* 21.7 (July 2026), p. 071003. ISSN: 1555-1415. DOI: 10.1115/1.4071568.

[18] J.H. Ginsberg. *Engineering Dynamics, 3rd edition*. Cambridge University Press, 2008.

[19] Paulo Flores et al. “On the continuous contact force models for soft materials in multibody dynamics”. In: *Multibody System Dynamics* 25.3 (2011), pp. 357–375. DOI: 10.1007/s11044-010-9237-4.

[20] K. H. Hunt and F. R. E. Crossley. “Coefficient of Restitution Interpreted as Damping in Vibroimpact”. In: *Journal of Applied Mechanics* 42.2 (June 1975), pp. 440–445. ISSN: 0021-8936. DOI: 10.1115/1.3423596.

[21] H. M. Lankarani and P. E. Nikravesh. “A Contact Force Model With Hysteresis Damping for Impact Analysis of Multibody Systems”. In: International Design Engineering Technical Conferences and Computers and Information in Engineering Conference. Montreal, Canada, Sept. 1989, pp. 45–51. DOI: 10.1115/DETC1989-0104.

[22] Shiwu Hu and Xinglin Guo. “A dissipative contact force model for impact analysis in multibody dynamics”. In: *Multibody System Dynamics* 35.2 (2015), pp. 131–151. DOI: 10.1007/s11044-015-9453-z.